catalysts

MDPI

Article

Coupling Interface Construction of $Ni(OH)_2/MoS_2$ Composite Electrode for Efficient Alkaline Oxygen Evolution Reaction

Ge Liu [1], Xuezhi Ouyang [1], Xue-Ling Wei [2,*], Wei-Wei Bao [2], Xiao-Hua Feng [1] and Jun-Jun Zhang [1,3,*]

[1] School of Materials Science and Chemical Engineering, Xi'an Technological University, Xi'an 710021, China
[2] National & Local Joint Engineering Laboratory for Slag Comprehensive Utilization and Environmental Technology, School of Material Science and Engineering, Shaanxi University of Technology, Hanzhong 723000, China
[3] State Key Laboratory of High-Efficiency Utilization of Coal and Green Chemical Engineering, College of Chemistry & Chemical Engineering, Ningxia University, Yinchuan 750021, China
* Correspondence: weixueling@snut.edu.cn (X.-L.W.); zhangjunjun@xatu.edu.cn (J.-J.Z.)

Abstract: The transition metal-based catalysts have excellent electrochemical oxygen evolution reaction catalytic activity in alkaline electrolytes, attracting a significant number of researchers' attention. Herein, we used two-step hydrothermal and solvothermal methods to prepare a $Ni(OH)_2/MoS_2/NF$ electrocatalyst. The electrocatalyst displayed outstanding OER activity in 1.0 M KOH electrolyte with lower overpotential (296 mV at 50 $mA \cdot cm^{-2}$) and remarkable durability. Comprehensive analysis shows that reinforcement of the catalytic function is due to the synergistic effect between $Ni(OH)_2$ and MoS_2, which can provide more highly active sites for the catalyst. This also provides a reliable strategy for the application of heterogeneous interface engineering in energy catalysis.

Keywords: oxygen evolution reaction; solvothermal; $Ni(OH)_2/MoS_2$; heterostructures; synergistic effect; electrocatalyst

Citation: Liu, G.; Ouyang, X.; Wei, X.-L.; Bao, W.-W.; Feng, X.-H.; Zhang, J.-J. Coupling Interface Construction of $Ni(OH)_2/MoS_2$ Composite Electrode for Efficient Alkaline Oxygen Evolution Reaction. *Catalysts* **2022**, *12*, 966. https://doi.org/10.3390/catal12090966

Academic Editors: Bing Zhang and Chuntian Qiu

Received: 5 August 2022
Accepted: 26 August 2022
Published: 29 August 2022

1. Introduction

The increasing use of energy consumption and serious environmental pollution have forced us to look for renewable energy [1,2]. Hydrogen is considered a promising energy source because of its low cost, sustainability and high energy density [3,4]. Currently, hydrogen production by electrolysis of water is considered to be the most efficient method [5,6]. The water splitting process can be divided into two reactions: oxygen evolution reaction (OER) and hydrogen evolution reaction [7,8]. However, the OER involves four electron and proton transfer processes, more energy needs to be expended than HER [9,10]. In general, catalysts can effectively lower the energy barrier required for the reaction [11]. For example, Pt-based catalysts, Ir-based catalysts and other noble metal catalysts have excellent catalytic activity. Nevertheless, noble metal catalysts are expensive due to their limited reserves on the Earth, which restrict their large-scale commercial applications [12,13]. Therefore, there is a need to develop highly active, inexpensive, durable and stable metal-based catalysts [14,15].

Transition metal hydroxides have the advantages of simple synthesis, low production cost and excellent electrochemical performance [16,17]. Nickel hydroxides are considered to be a good catalyst for water electrolysis [18]. However, the poor electronic conductivity and slow ion transfer rate of single transition metal hydroxides hinder further performance optimization [19,20]. Transition metal dihalide (MX_2, M stands for transition metal, X stands for chalcogenides S, Te or Se) have attracted enormous attention due to their high electrochemical performance [21]. MoS_2 is deemed to a promising non-noble metal catalyst [22,23]. MoS_2 possess a lamellar configuration with feeble interlayer van der Waals forces [24]. At present, MoS_2 is widely used as an electrocatalyst for hydrogen production because of its excellent HER performance [25]. Theoretical calculation shows that the MoS_2

active sites for HER are at the edge [26]. A large number of unsaturated sulfur atoms at the edge can easily adsorb H, generating hydrogen on the surface of MoS_2 [21,27]. Similarly, the OER active center of MoS_2 is also located at the edge [28]. It has been reported that MoS_2 can be used to enhance the OER activity through heteroatom-doping, changing the electronic structure, and constructing a hetero-cooperative interface [6,29–31]. Moreover, the intrinsic conductivity and surface electronic structure of electrocatalysts determine the level of electrochemical activity [32]. In general, the heterostructures formed can adjust their electronic configuration and thus improve electrical conductivity [19–23,33,34].

Based on the above understandings, in this paper, a $Ni(OH)_2/MoS_2$/NF composite electrode was constructed using the two-step hydrothermal and solvothermal methods for OER. The 50 and 100 $mA{\cdot}cm^{-2}$ current density correspond to the 296 and 314 mV overpotential. The prominent electrochemical function comes from the self-supporting effect of NF and the synergistic effect of the formed heterostructures. It provides an idea for the subsequent preparation of non-noble metal catalysts with heterostructures structures for OER.

2. Results

Here, the $Ni(OH)_2/MoS_2$/NF composite electrode was fabricated using the two-step hydrothermal/solvothermal method, as shown in Figure 1. $Ni(OH)_2$ three dimensional arrays were anchored on NF by simple hydrothermal method. Further, the MoS_2 substance was grown on $Ni(OH)_2$ nanosheets through the secondary solvothermal process. The specific experimental process can be seen in the Supplementary Materials. The $Ni(OH)_2$ nanosheets were grown directly on the NF, avoiding use of binders and providing more active area. Additionally, the $Ni(OH)_2$ nanosheets are overlapped, providing more load position for the granular MoS_2 [35]. The heterostructures can not only enhance the catalytic activity of the catalyst by electron transfer between different components, but also increase the number of active centers [36,37]. The XRD measurement peaks of the powders collected in the first step belonged to $Ni(OH)_2$ powders, corresponding to JCPDS NO. 38-0715 (Figure S1), indicating that $Ni(OH)_2$ was successfully prepared. The XRD measurement peaks of the powders collected in the second step belonged to the MoS_2 phase. The peak at (002) is significantly shifted compared to the standard card, probably because of a small change in the interlayer spacing [29].

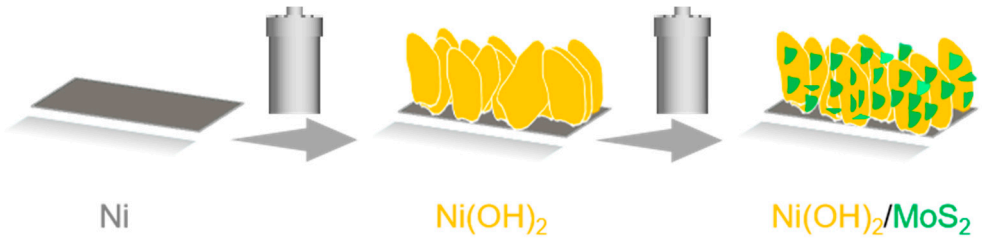

Figure 1. Schematic illustration of the synthesis.

The microstructure of the electrode was investigated by scanning electron microscopy (SEM) and transmission electron microscopy (TEM). NFs are interconnected three-dimensional network structures and have a smooth surface (Figure S3). $Ni(OH)_2$/NF exhibits a layer-by-layer stack of thin nanosheet structures (Figure S4). The MoS_2/NF electrode exhibits flower-like structure assembled by uniformly distributed nanosheets (Figure S5). Figure 2a and Figure S6 show that the $Ni(OH)_2/MoS_2$/NF composite electrode has the structure of $Ni(OH)_2$ and MoS_2, which can preliminarily determine the required composite electrode. Apparently, the small MoS_2 assemblies grows on the large two-dimensional $Ni(OH)_2$ lamellar structure, which can provide many composite interfaces and thus enhance the synergistic effect of the heterostructure [38,39]. We can adjust the proportion of components to prepare catalytic samples with different proportions (Figure S7). Figure 2b exhibits the TEM image of $Ni(OH)_2/MoS_2$/NF. $Ni(OH)_2$ is a lami-

nated structure and MoS_2 assemblies are covered on the nanosheets. It can be measured from Figure 2c that the lattice spacing of 0.405 nm and 0.610 nm correspond to the (006) crystal face of $Ni(OH)_2$ and (002) crystal face of MoS_2, respectively. The results further prove that we have obtained the electrode with heterogeneous $Ni(OH)_2$ and MoS_2 structure. Figure 3 is an elemental mapping images of duan electrode, in which Ni, Mo, S and O elements are evenly distributed in the composite structure. Meanwhile, combing the SEM image and TEM image, successful preparation of integrated electrodes was demonstrated.

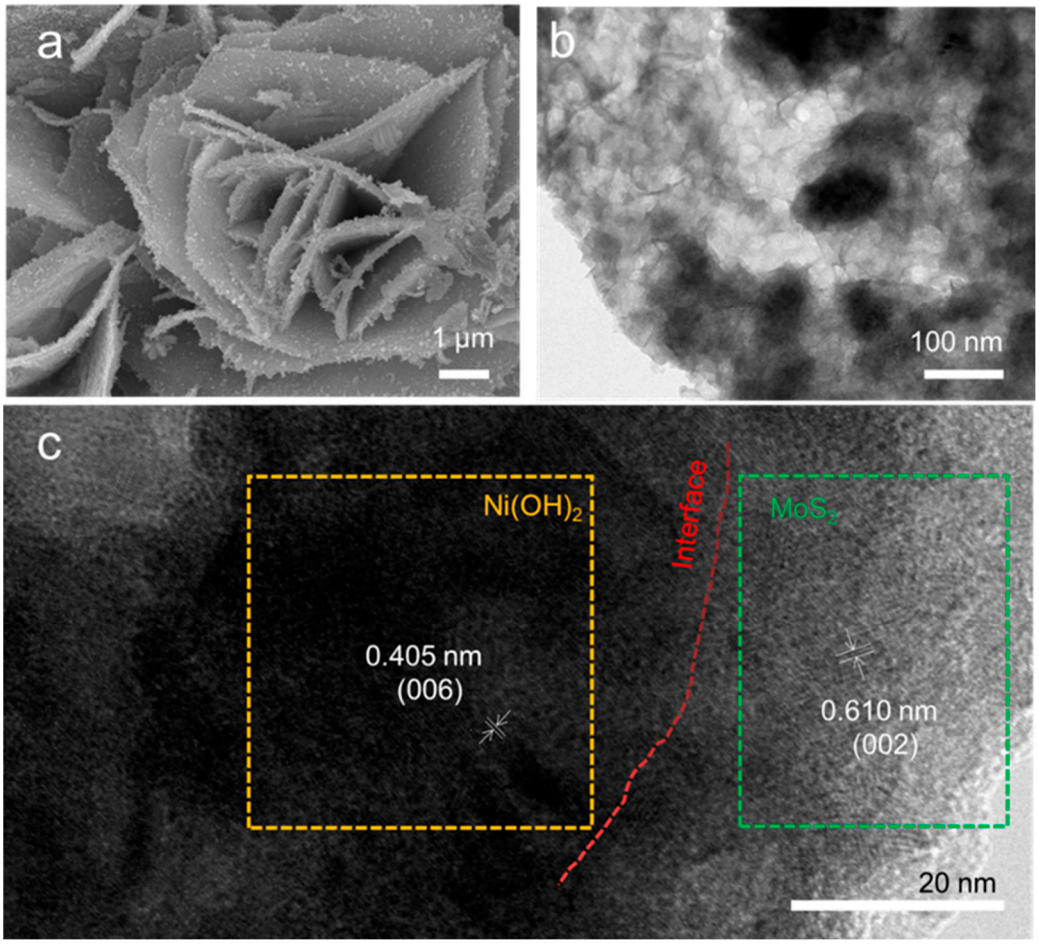

Figure 2. (**a**) SEM image, (**b**) TEM image, (**c**) HR-TEM image of the $Ni(OH)_2/MoS_2$/NF electrocatalysts.

The OER performance of composite electrodes was tested. Simultaneously, the catalytic ability of $Ni(OH)_2$/NF, MoS_2/NF and bare NF were contrasted (see Supplementary Materials for details). The polarization curve results show that the dual $Ni(OH)_2/MoS_2$/NF electrode has the best OER catalytic activity contrasted with other comparative electrodes (Figure 4a). Figure 4b shows that the overpotential of each electrode at 50 and 100 $mA{\cdot}cm^{-2}$ current outputs. Generally speaking, the lower the overpotential, the better the catalytic performance [36]. Compared with the individual $Ni(OH)_2$ or MoS_2 catalyst, the $Ni(OH)_2/MoS_2$/NF exhibits the smallest overpotentials (296 mV at 50 $mA{\cdot}cm^{-2}$ current output, 314 mV at 100 $mA{\cdot}cm^{-2}$). Furthermore, the overpotential is smaller in contrast with many reported water oxidation electrocatalysts, such as $Ti@NiCo_2O_4$ (353 mV at 10 $mA{\cdot}cm^{-2}$), CoCr LDH (340 mV at 10 $mA{\cdot}cm^{-2}$) and Ni/NiO (470 mV at 10 $mA{\cdot}cm^{-2}$), for details see Supplementary Table S1 and Figure 5.

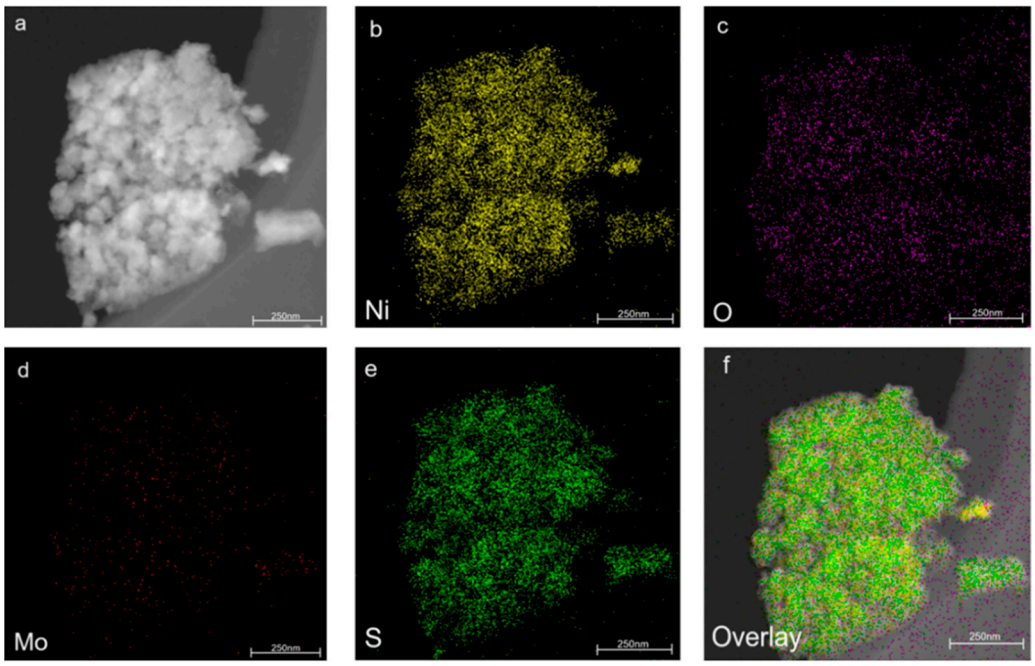

Figure 3. The corresponding element mapping of $Ni(OH)_2/MoS_2/NF$ electrocatalysts: (**a**) STEM image; (**b**) Nickel; (**c**) Oxygen; (**d**) Molybdenum; (**e**) sulfur; (**f**) Overlay.

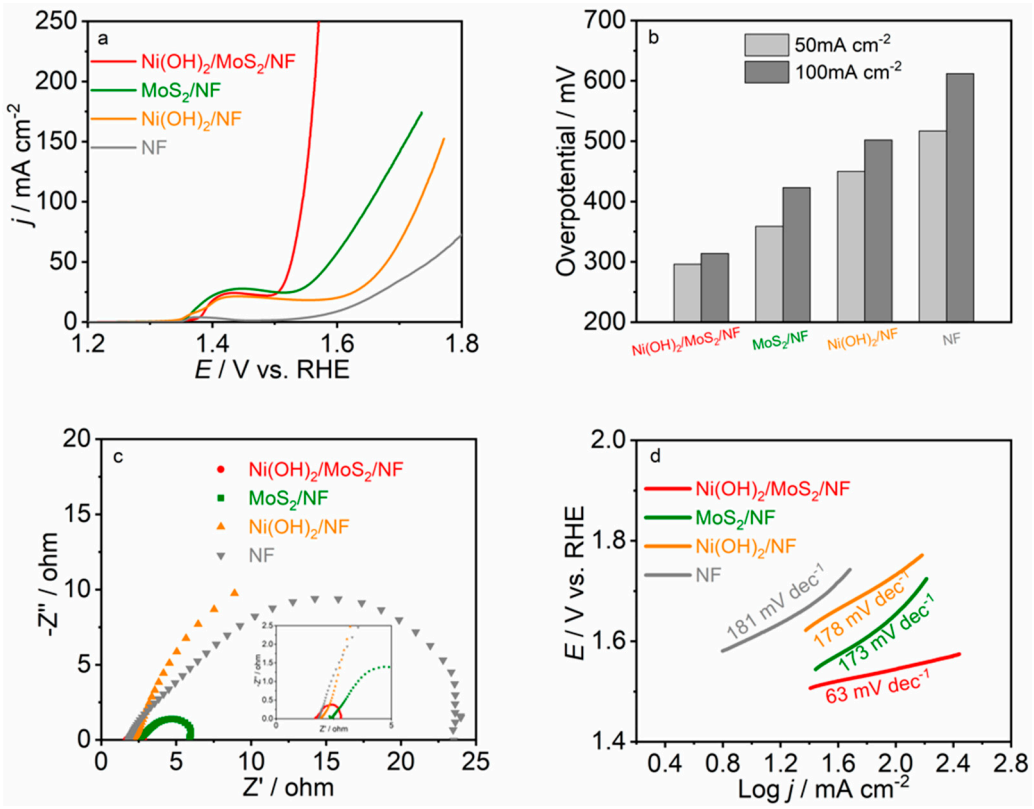

Figure 4. (**a**) The iR-corrected polarization curves (**b**) a comparison of the corresponding overpotentials at 50 $mA{\cdot}cm^{-2}$ and 100 $mA{\cdot}cm^{-2}$ current outputs, (**c**) the electrochemical impedance spectroscopy (**d**) corresponding Tafel plot of the $Ni(OH)_2/MoS_2/NF$, MoS_2/NF, $Ni(OH)_2/NF$ and bare NF electrodes.

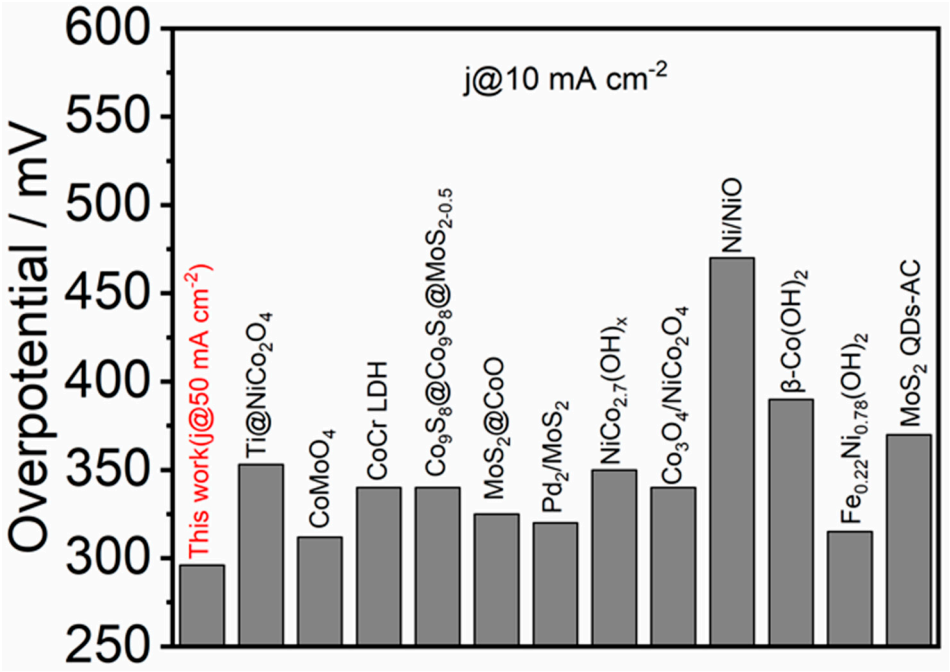

Figure 5. The comparison of OER performance for some representative non-noble electrocatalysts.

Electrochemical impedance spectroscopy (EIS) can describe the interface properties between electrode and the electrolyte, and it is a powerful means to indicate interfacial charge transfer. The size of the arc in the EIS is related to the electrode surface charge transfer resistance. The small arc radius in the EIS represents the small charge transfer resistance of the catalytic electrode, and also represents the fast dynamic response [40,41]. As show in Figure 4c, the arc size of the dual electrode is smallest, indicating its robust catalytic reaction kinetics. The small Tafel slope means a favorable electron transfer rate and a faster water oxidation rate [42]. As shown in Figure 4d, the $Ni(OH)_2/MoS_2/NF$ possesses the smallest Tafel slope (63 $mV \cdot dec^{-1}$), indicating the robust catalytic kinetics of water oxidation [43].

Stability is an indicator of whether the catalyst can be used commercially on a large scale [44]. The stability of the composite electrode was tested using multi-step potential and multi-step current methods, as shown in Figure 6a,b, the $Ni(OH)_2/MoS_2/NF$ has excellent stability. Cyclic voltammetry (CV) is an important standard to verify the durability. Figure 6c depicts the polarization curves before and after 500 CV cycles. It can be seen that the polarization curve does not change significantly. The EIS spectra in Figure 6d also exhibit the same result, indicating that the catalytic electrode has excellent stability. In the meantime, the chronoamperometric test was performed on the composite electrode. After 15 h of operation at constant potential, the composite electrode did not appear to have obvious decay (Figure S8). We studied the morphology and structure of the electrode before and after the test, and the morphology and electronic structure of the electrode can be maintained well after a long time running (Figures S9 and S10).

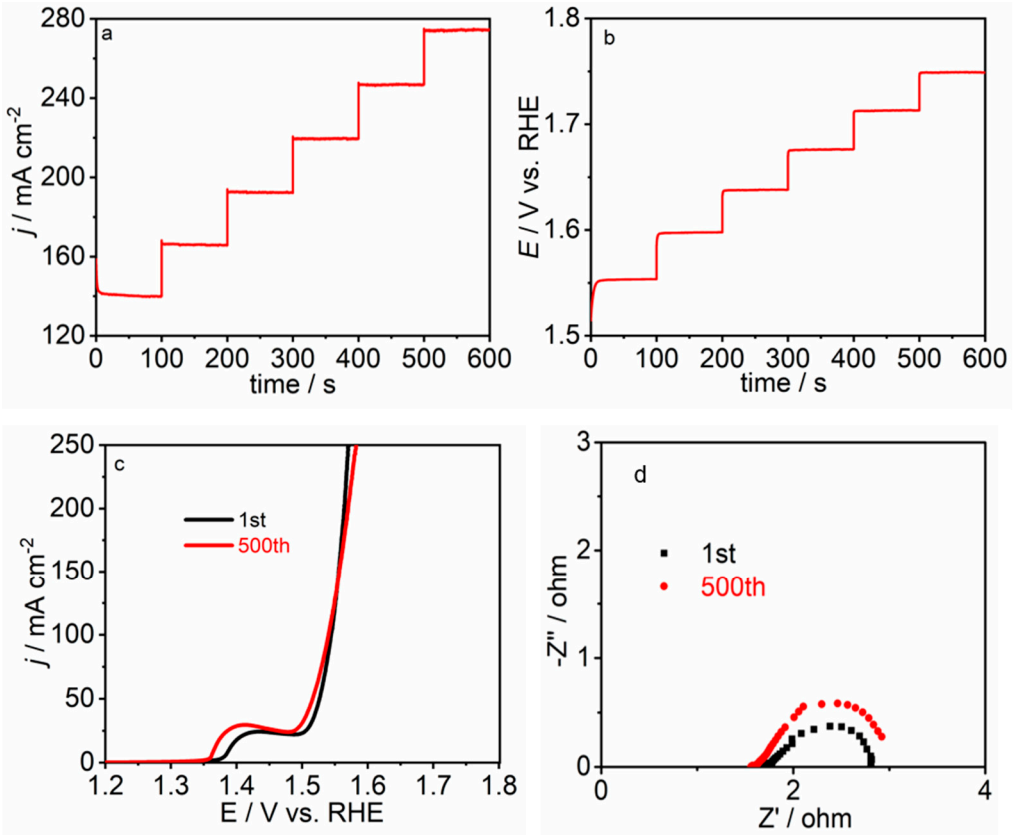

Figure 6. (**a**) The multi-potential steps (**b**) the multi-current steps (**c**) the polarization curves of the $Ni(OH)_2/MoS_2$/NF electrode before and after 500 cycles cyclic voltammetry (**d**) electrochemical impedance spectra of $Ni(OH)_2/MoS_2$/NF electrode before and after 500 cycles of cyclic voltammetry.

3. Discussion

The element valence states were analyzed using X-ray photoelectron spectroscopy (Figure S11). To ulteriorly comprehend the reason of activity enhancement, the XPS spectra of single component and composite electrodes were compared, as shown in Figure 7. In the XPS spectrum of Ni 2p, there are two main peaks (855.4 and 873 eV), corresponding to Ni $2p_{3/2}$ and Ni $2p_{1/2}$ of Ni^{2+} (Figure S11b) [45]. This result further confirms the existence of $Ni(OH)_2$ [46]. Moreover, compared with the $Ni(OH)_2$ electrode, the peaks of Ni $2p_{3/2}$ and Ni $2p_{1/2}$ in composite electrode are shifted to higher energy. Figure 7b is the XPS spectrum of Mo 3d. The peak at 232.56 eV is Mo $3d_{3/2}$ orbital. The peak at 234.84 eV is assigned to Mo^{6+} (Figure S11c) [47]. Comparing the Mo 3d of MoS_2/NF and the combined electrode, it can be seen that the peak of Mo $3d_{3/2}$ has shifted to a lower energy. The phenomenon of peak shift indicates that the electron density of Ni and Mo ions has changed, and electron transfer has occurred in $Ni(OH)_2/MoS_2$/NF electrode [48]. According to the change of electron density, we can preliminarily determine that part of electron transfer from $Ni(OH)_2$ to MoS_2 occurred at the interface of the composite electrode [49]. The representative peaks (160.92 eV and 162.03 eV) correspond to S $2p_{3/2}$ and S $2p_{1/2}$. The nearby peak at 163.00 eV is S_2^{2-}, indicating the existence of MoS_2. More importantly, the peak (168.90 eV) proves the existence of the S-Ni bond. [50]. This result strongly suggests an interface between $Ni(OH)_2$ and MoS_2. The C 1s and O 1s peaks in the composite electrode were also analyzed and the results were presented in the Supplementary Material (Figure S11e,f). These results all indicate electron redistribution at the interface of the catalytic electrode, which can effectively expedite the rate of the reaction process and achieve higher catalytic activity. Furthermore, the electrochemical active area was measured (Figure S12). It was found that the $Ni(OH)_2/MoS_2$/NF composite electrode has a larger active area than the $Ni(OH)_2$ electrode.

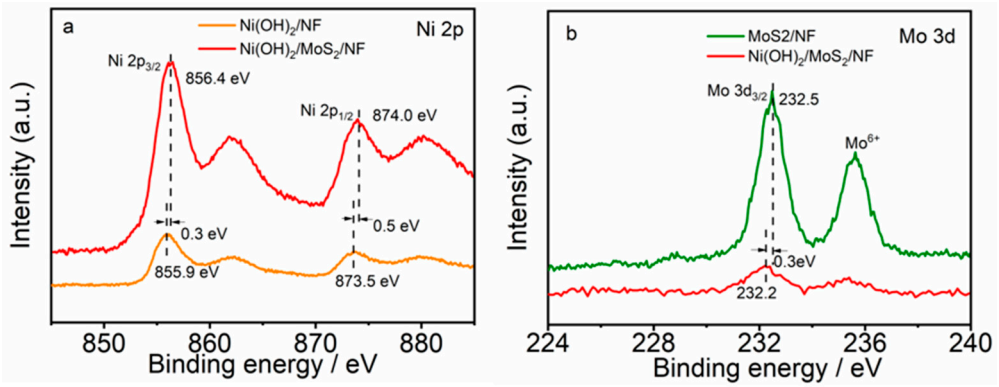

Figure 7. XPS spectra of (**a**) Ni 2p, (**b**) Mo 3d of $Ni(OH)_2$, MoS_2 and $Ni(OH)_2/MoS_2$/NF electrodes.

4. Materials and Methods

4.1. Materials

Nickel nitrate hexahydrate ($Ni(NO_3)_2{\cdot}6H_2O$), urea ($CO(NH_2)_2$) and ammonium fluoride (NH_4F) were purchased from Tianjin Damao Chemical Reagent Factory (Tianjin, China). Ammonium tetrathiomolybdate ($(NH_4)_2MoS_4$) and DMF were purchased from Aladdin Biochemical Technology Co., Ltd. (Shanghai, China). Nickel foam (NF) was used as the substrate. The thickness of the NF is about 1 mm. NF was firstly washed with HCl solution under ultrasonic, ethanol and water several times to remove the surface impurities. All the chemicals were used without further purification.

4.2. Materials Synthesis

Synthesis of $Ni(OH)_2$/NF. An aqueous solution (25 mL) containing 1.5 mmol (0.436 g) $Ni(NO_3){\cdot}6H_2O$, 7.5 mmol (0.455 g) $CO(NH_2)_2$ and 4 mmol (0.148 g) NH_4F was treated with ultrasound to accelerate dissolution. Then, the solution was encapsulated into the 50 mL PTFE-lined stainless steel reactor, and the pre-treated Ni foam was placed against the inner wall of the reactor. The reaction temperature and time were set as 120 °C and 4 h, respectively. At the end of the reaction, the nickel substrate was cleaned and dried. Powder samples from the bottom of the reactor were also collected.

Synthesis of $Ni(OH)_2/MoS_2$/NF. An amount of 0.021 g $(NH4)_2MoS_4$ and 35 mL DMF were added into a 50 mL PTFE-lined stainless steel reactor. Then, $Ni(OH)_2$/NF was placed against the inner wall of the reactor. The reaction temperature and time were set as 200°C and 10 h, respectively. The MoS_2/NF electrode was prepared by the similar method. When the quantity of $(NH_4)_2MoS_4$ was set to 0.013 g and 0.030 g, the obtained samples were labeled as $Ni(OH)_2/MoS_2$/NF-13 and $Ni(OH)_2/MoS_2$/NF-30.

4.3. Materials Characterizations

XRD pattern measurements were performed using a Bruker D8 X-ray diffractometer (Bruker AXS GmbH, Karlsruhe, Germany) using Cu Kα radiation (40 kV, 30 mA, λ = 1.5406 Å). The SEM images were collected on JSM-7610F (JEOL, Tokyo, Japan) scanning electron microscope at 10 kV. TEM and HRTEM images were performed using a JEM-F200 (JEOL, Tokyo, Japan) microscope. XPS measurements were performed using the Axis Ultra DLD (Kratos, Stretford, UK) X-ray photoelectron spectrometer.

4.4. Electrochemical Characterizations

Electrochemical tests were all acquired on a CHI-660E electrochemical workstation (CHI Instruments, Shanghai, China) using a standard three-electrode system. $Ni(OH)_2/MoS_2$/NF electrodes, carbon rods and a Hg/HgO electrode served as work electrodes, counter electrode and reference electrode, respectively. The electrolyte was 1.0 M KOH. The linear sweep voltammetry (LSV) curve was scanned at a rate of 10 mV/s and calibrated using iR correction. The measurement frequency range for electrochemical impedance spectroscopy (EIS) was 0.1 to 105 Hz. The Overpotential η (mV) = ((E vs. RHE) − 1.23) × 1000.

The potential was converted to the potential versus the reversible hydrogen electrode (RHE) using the relationship, $E_{RHE} = E_{Hg/HgO} + E^0{}_{Hg/HgO} + 0.059$ pH. $E^0{}_{Hg/HgO} = 0.098$V (25 °C).

5. Conclusions

In summary, we constructed a $Ni(OH)_2/MoS_2$/NF composite electrode with heterostructures using two-step hydrothermal/solvothermal methods. The $Ni(OH)_2/MoS_2$/NF electrode displayed excellent oxygen evolution reaction performance. The $Ni(OH)_2/MoS_2$/NF possesses lower overpotential (296 mV at 50 mA·cm^{-2}) and Tafel slope (63 mV·dec^{-1}). The good OER performance is ascribed to the synergistic effect of composite interface, which accelerates the electron transport and increases the OER rate of the water splitting process. The method can be applied to other interface engineering to design OER catalytic electrodes.

Supplementary Materials: The following supporting information can be downloaded at: https://www.mdpi.com/article/10.3390/catal12090966/s1, Figure S1. The XRD pattern of $Ni(OH)_2$ powder. Figure S2. The XRD pattern of MoS_2 powder. Figure S3. High resolution scanning electron microscopy with NF at different magnifications. Figure S4. High resolution scanning electron microscopy of $Ni(OH)_2$/NF at different magnifications. Figure S5. High resolution scanning electron microscopy of MoS_2/NF at different magnifications. Figure S6. High resolution scanning electron microscopy of $Ni(OH)_2/MoS_2$/NF at different magnifications. Figure S7. Scanning electron microscopy images of (a) $Ni(OH)_2/MoS_2$/NF-13 and (b) $Ni(OH)_2/MoS_2$/NF-30 electrodes. Figure S8. The chronoamperometry measurement of $Ni(OH)_2/MoS_2$/NF composite electrodes. Figure S9. High-resolution XPS (a) Ni 2p, (b) Mo 3d, (c) S 2p and (d) O 1s of $Ni(OH)_2/MoS_2$/NF electrode before and after long-time stability test. Figure S10. The SEM image of $Ni(OH)_2/MoS_2$/NF electrode after long-time stability test. Figure S11. (a) XPS survey spectra, (b) Ni 2p, (c) Mo 3d, (d) S 2p, (e) C 1s and (f) O 1s of $Ni(OH)_2/MoS_2$/NF electrode. Figure S12. CV curves of the (a) $Ni(OH)_2$/NF and (b) $Ni(OH)_2/MoS_2$/NF electrodes measured at different scan rates from 20 to 100 mV s^{-1} in a potential window without faradaic processes. (c) Plots of the current density vs. the scan rates for $Ni(OH)_2$/NF and $Ni(OH)_2/MoS_2$/NF electrodes. Table S1. Comparison of OER performance of $Ni(OH)_2/MoS_2$/NF catalyst with other reports. References [51–62] are cited in the Supplementary Materials.

Author Contributions: Conducted the synthesis of the electrodes and carried out corresponding characterizations, G.L. and X.-L.W.; writing—review and editing, helped to conduct data analysis and revised the manuscript, W.-W.B., X.-H.F. and X.O.; conceptualization, J.-J.Z.; analysis, J.-J.Z.; funding acquisition J.-J.Z.; writing—original draft J.-J.Z. All authors have read and agreed to the published version of the manuscript.

Funding: This work was supported by the National Natural Science Foundation of China (Grant No. 21902123), the Fundamental Research Fund for the Undergraduate Innovation Project (S202110702085) and the support of the Research Fund for the Doctoral Program of Xi'an Technological University (Grant No. 0853-302020540).

Institutional Review Board Statement: Not applicable.

Informed Consent Statement: Not applicable.

Data Availability Statement: The data presented in this study are available on request from the corresponding author.

Acknowledgments: We thank the funding support from the Science Funding Committee of China and the Science, Xi'an Technological University and Undergraduate Innovation Project.

Conflicts of Interest: The authors declare no conflict of interest.

References

1. Zhang, J.-J.; Li, M.-Y.; Li, X.; Bao, W.-W.; Jin, C.-Q.; Feng, X.-H.; Liu, G.; Yang, C.-M.; Zhang, N.-N. Chromium-modified ultrathin CoFe LDH as high-efficiency electrode for hydrogen evolution reaction. *Nanomaterials* **2022**, *12*, 1227. [CrossRef] [PubMed]
2. Li, X.; Liu, Y.-M.; Zhang, J.-J.; Yan, B.; Jin, C.-Q.; Dou, J.-J.; Li, M.-Y.; Feng, X.-H.; Liu, G. No Annealing Synthesis of Ordered Intermetallic PdCu Nanocatalysts for Boosting Formic Acid Oxidation. *Chem. Mater.* **2022**, *34*, 1385–1391. [CrossRef]

3. Lao, J.; Li, D.; Jiang, C.-L.; Luo, R.; Peng, H.; Qi, R.-J.; Lin, H.-C.; Huang, R.; Waterhouse, G.I.N.; Luo, C.H. Efficient overall water splitting using nickel boride-based electrocatalysts. *Int. J. Hydrog. Energy* **2020**, *45*, 28616–28625. [CrossRef]
4. Wang, J.-S.; Zhang, Z.-F.; Song, H.-R.; Zhang, B.; Liu, J.; Shai, X.-X.; Miao, L. Water dissociation kinetic-oriented design of nickel sulfides via tailored dual sites for efficient alkaline hydrogen evolution. *Adv. Funct. Mater.* **2021**, *31*, 2008578. [CrossRef]
5. Sun, M.; Zhang, Q.; Chen, Q.; Hou, X.; Peng, W.; Li, Y.; Zhang, F.; Xia, Q.; Fan, X. Coupling $LaNiO_3$ Nanorods with FeOOH Nanosheetsfor Oxygen Evolution Reaction. *Catalysts* **2022**, *12*, 594. [CrossRef]
6. Ai, T.-T.; Wang, H.-H.; Bao, W.-W.; Feng, L.-L.; Zou, X.-Y.; Wei, X.-L.; Ding, L.; Deng, Z.-F.; Rao, B. Fe-V synergistic doping effect of hierarchical Ni_3S_2 oblate-nanorod arrays for efficient electrocatalytic oxygen evolution reaction. *Chem. Eng. J.* **2022**, *450*, 138358. [CrossRef]
7. Liu, S.-Q.; Wen, H.-R.; Guo, Y.; Zhu, Y.-W.; Fu, X.-Z.; Sun, R.; Wong, C.-P. Amorphous $Ni(OH)_2$ encounter with crystalline CuS in hollow spheres: A mesoporous nano-shelled heterostructure for hydrogen evolution electrocatalysis. *Nano Energy* **2018**, *44*, 7–14. [CrossRef]
8. Xiao, G.; Chen, W.; Cai, Y.; Zhang, S.; Wang, D.; Cai, D. FacileSynthesis of Sulfate-IntercalatedCoFe LDH Nanosheets Derived fromTwo-Dimensional ZIF-9(III) forPromoted Oxygen Evolution Reaction. *Catalysts* **2022**, *12*, 688. [CrossRef]
9. Yan, Q.; Liu, Z.; Bai, X.; Zhang, X.; Gao, R.; Yuan, W.; Chen, Z.; Li, Z.; Li, Y. In situ formed edge-rich Ni_3S_2-NiOOH heterojunctions for oxygen evolution reaction. *J. Electrochem. Soc.* **2022**, *169*, 054532. [CrossRef]
10. Liang, Z.-J.; Lu, Y.-C. Critical role of redox mediator in suppressing charging instabilities of lithium−oxygen batteries. *J. Am. Chem. Soc.* **2016**, *138*, 7574–7583. [CrossRef]
11. Zhang, M.-L.; Zhan, Y.-Q.; Ye, L.; Guo, B.-W.; Gong, Y.-Q. Hierarchically constructed Ag nanowires shelled with ultrathin Co-LDH nanosheets for advanced oxygen evolution reaction. *Appl. Catal. B* **2021**, *298*, 120601. [CrossRef]
12. Du, X.-Q.; Ma, G.-Y.; Zhang, X.-S. Oxygen vacancy-confined $CoMoO_4$@$CoNiO_2$ nanorod arrays for oxygen evolution with improved performance. *Dalton Trans.* **2019**, *48*, 10116–10121. [CrossRef]
13. Fei, B.; Chen, Z.-L.; Liu, J.-X.; Xu, H.-B.; Yan, X.-X.; Qing, H.-L.; Chen, M.; Wu, R.B. Ultrathinning nickel sulfide with modulated electron density for efficient water splitting. *Adv. Energy Mater.* **2020**, *10*, 2001963. [CrossRef]
14. Zhang, J.-J.; Yang, C.-M.; Jin, C.-Q.; Bao, W.-W.; Nan, R.-H.; Hu, L.; Liu, G.; Zhang, N.-N. Hierarchical iron molybdate nanostructure array for efficient water oxidation through optimizing electron density. *Chem. Commun.* **2021**, *57*, 3563–3566. [CrossRef]
15. Wang, X.; Liu, W.; Wang, J.-N.; Li, C.-M.; Zheng, R.K.; Zhang, H.X.; Liu, J.Q.; Zhang, X.W. Cobalt and vanadium co-doped FeOOH nanoribbons: An iron-rich electrocatalyst for efficient water oxidation. *Mater. Chem. Front.* **2021**, *5*, 6485–6490. [CrossRef]
16. Sun, F.-Z.; Li, C.-Q.; Li, B.; Lin, Y.-Q. Amorphous MoSx developed on $Co(OH)_2$ nanosheets generating efficient oxygen evolution catalyst. *J. Mater. Chem. A* **2017**, *5*, 23103–23114. [CrossRef]
17. Gu, L.-F.; Li, C.-F.; Zhao, J.-W.; Xie, L.-J.; Wu, J.-Q.; Ren, Q.; Li, G.-R. Dual modulation of lattice strain and charge polarization induced by $Co(OH)_2$/$Ni(OH)_2$ interfaces for efficient oxygen evolution catalysis. *J. Mater. Chem. A* **2021**, *9*, 13279–13287. [CrossRef]
18. Cao, Q.-H.; Luo, M.; Huang, Y.-T.; Liu, Q.; Kong, X.-X.; Lei, J.-L.; Jiang, Z.; Wang, J.H. Temperature and doping-tuned coordination environments around electroactive centers in Fe-doped α(β)-$Ni(OH)_2$ for excellent water splitting. *Sustain. Energy Fuels* **2020**, *4*, 1522–1531. [CrossRef]
19. Shi, D.-W.; Zhang, L.-Y.; Zhang, N.-D.; Zhang, Y.-W.; Yu, Z.-G.; Gong, H. Boosted electrochemical property from surface engineering of ultrathin interlaced $Ni(OH)_2$ nanosheets with $Co(OH)_2$ quantum dot modification. *Nanoscale* **2018**, *10*, 10554–10563. [CrossRef]
20. Aguilera, L.; Leyet, Y.; Almeida, A.; Moreira, J.A.; de la Cruz, J.P.; Milán-Garcés, E.A.; Passos, R.R.; Pocrifka, L.A. Electrochemical preparation of $Ni(OH)_2$/CoOOH bilayer films for application in energy storage devices. *J. Alloys Compd.* **2021**, *874*, 159858. [CrossRef]
21. Chen, S.-R.; Yin, Z.-H.; Cui, M.; Liu, X.; Xiong, J.-B.; Li, Y.-Q.; Ma, T.L. Interface engineering of transitional metal sulfides-MoS_2 heterostructure composites as effective electrocatalysts for water-splitting. *J. Mater. Chem. A* **2021**, *9*, 2070–2092.
22. Mansingh, S.; Das, K.K.; Parida, K. HERs in an acidic medium over MoS_2 nanosheets: From fundamentals to synthesis and the recent progress. *Sustain. Energy Fuels* **2021**, *5*, 1952–1987. [CrossRef]
23. Ren, Y.-X.; Zhu, S.-L.; Liang, Y.-Q.; Li, Z.-Y.; Wu, S.-L.; Chang, C.-T.; Luo, S.-Y.; Cui, Z.D. Hierarchical Ni_3S_4@MoS_2 nanocomposites as efficient electrocatalysts for hydrogen evolution reaction. *J. Mater. Sci.* **2021**, *95*, 70–77. [CrossRef]
24. Wang, H.-M.; Li, C.-H.; Fang, P.-F.; Zhang, Z.-L.; Zhang, J.-Z. Synthesis, properties, and optoelectronic applications of two-dimensional MoS_2 and MoS_2-based heterostructures. *Chem. Soc. Rev.* **2018**, *47*, 6101–6127. [CrossRef]
25. Jung, H.-Y.; Chae, M.-J.; Park, J.-H.; Song, Y.-I.; Ro, J.-C.; Suh, S.-J. Effect of platinum group metals on MoS_2 nanosheets for a high-performance hydrogen evolution reaction catalyst. *ACS Appl. Energy Mater.* **2021**, *4*, 10748–10755. [CrossRef]
26. Huang, J.-B.; Jiang, Y.; An, T.-Y.; Cao, M.-H. Increasing the active sites and intrinsic activity of transition metal chalcogenide electrocatalysts for enhanced water splitting. *J. Mater. Chem. A* **2020**, *8*, 25465–25498. [CrossRef]
27. Yu, F.; Yu, L.; Mishra, I.-K.; Yu, Y.; Ren, Z.-F.; Zhou, H.-Q. Recent developments in earth-abundant and non-noble electrocatalysts for water electrolysis. *Mater. Today Phys.* **2018**, *7*, 121–138. [CrossRef]
28. Huang, Y.-Z.; Huang, J.-C.; Xu, K.S.; Geng, R.-R. Constructing $NiSe_2$@MoS_2 nano-heterostructures on a carbon fiber paper for electrocatalytic oxygen evolution. *RSC Adv.* **2021**, *11*, 26928–26936. [CrossRef]

29. Jin, Q.; Liu, N.; Dai, C.-N.; Xu, R.-N.; Wu, B.; Yu, G.-Q.; Chen, B.-H.; Du, Y.-Z. H_2-Directing Strategy on In Situ Synthesis of Co-MoS_2 with Highly Expanded Interlayer for Elegant HER Activity and its Mechanism. *Adv. Energy Mater.* **2020**, *10*, 2000291. [CrossRef]
30. Tang, B.-S.; Yu, Z.-G.; Seng, H.-L.; Zhang, N.-D.; Liu, X.-X.; Zhang, Y.-W.; Yang, W.-F.; Gong, H. Simultaneous edge and electronic control of MoS_2 nanosheets through Fe doping for an efficient oxygen evolution reaction. *Nanoscale* **2018**, *10*, 20113–20119. [CrossRef] [PubMed]
31. Guan, S.-D.; Fu, X.-L.; Lao, Z.-Z.; Jin, C.-H.; Peng, Z.-J. NiS–MoS_2 hetero-nanosheet array electrocatalysts for efficient overall water splitting. *Sustain. Energy Fuels* **2019**, *3*, 2056–2066. [CrossRef]
32. Yu, M.-Q.; Moon, G.H.; Castillo, R.G.; DeBeer, S.; Weidenthaler, C.; Tüysüz, H. Dual role of silver moieties coupled with ordered mesoporous cobalt oxide towards electrocatalytic oxygen evolution reaction. *Angew. Chem. Int. Ed.* **2020**, *132*, 16687–16695.
33. Wang, Y.-Z.; Liu, S.-S.; Hao, X.-F.; Luan, S.-R.; You, H.-H.; Zhou, J.-S.; Song, D.-D.; Wang, D.; Li, H.; Gao, F.-M. Surface reorganization engineering of the N dopant MoS_2 construction heterostructures MoO_x@N-doped MoS_{2-x} by in-situ electrochemical oxidation activated for an efficient oxygen evolution reaction. *J. Mater. Chem. A* **2019**, *7*, 10572–10580. [CrossRef]
34. Priamushko, T.; Guillet-Nicolas, R.; Yu, M.; Doyle, M.; Weidenthaler, C.; Tüysüz, H.; Kleitz, F. Nanocast mixed Ni–Co–Mn oxides with controlled surface and pore structure for electrochemical oxygen evolution reaction. *ACS Appl. Energy Mater.* **2020**, *3*, 5597–5609. [CrossRef]
35. Yang, Y.-Q.; Zhang, K.; Lin, H.-L.; Li, X.; Chan, H.-C.; Yang, L.-C.; Gao, Q.S. $MoS_2-Ni_3S_2$ heteronanorods as efficient and stable bifunctional electrocatalysts for overall water splitting. *ACS Catal.* **2017**, *7*, 2357–2366. [CrossRef]
36. Zou, X.; Liu, Y.-P.; Li, G.-D.; Wu, Y.-Y.; Liu, D.-P.; Li, W.; Li, H.-W.; Wang, D.; Zhang, J.Y.; Zou, X.X. Ultrafast formation of amorphous bimetallic hydroxide films on 3D conductive sulfide nanoarrays for large-current-density oxygen evolution electrocatalysis. *Adv. Mater.* **2017**, *29*, 1700404. [CrossRef]
37. Li, X.; Kou, Z.-K.; Xi, S.-B.; Zang, W.-J.; Yang, T.; Zhang, L.; Wang, J. Porous $NiCo_2S_4$/FeOOH nanowire arrays with rich sulfide/hydroxide interfaces enable high OER activity. *Nano Energy* **2020**, *78*, 105230. [CrossRef]
38. Li, S.-M.; Yu, Y.-M.; Sun, X.-Y.; Ding, X.-F.; Yang, H.-F.; Pan, S.-B.; Wang, L.X.; Zhang, Q.T. Enhanced electronic interaction in hemin@$Ni(OH)_2$ composite for efficient electrocatalytic oxygen evolution. *J. Alloys Compd.* **2022**, *892*, 161780. [CrossRef]
39. Dua, X.-Q.; Yang, Z.; Li, Y.; Gong, Y.-Q.; Zhao, M. Controlled synthesis of $Ni(OH)_2/Ni_3S_2$ hybrid nanosheet arrays as highly active and stable electrocatalysts for water splitting. *J. Mater. Chem. A* **2018**, *6*, 6938–6946. [CrossRef]
40. Xi, W.-G.; Yan, G.; Tan, H.-Q.; Xiao, L.-G.; Cheng, S.-H.; Khan, S.-U.; Wang, Y.-H.; Lia, Y.G. Superaerophobic P-doped $Ni(OH)_2/NiMoO_4$ hierarchical nanosheet arrays grown on Ni foam for electrocatalytic overall water splitting. *Dalton Trans.* **2018**, *47*, 8787–8793. [CrossRef]
41. Lu, Y.-K.; Liu, C.-C.; Xing, Y.-Y.; Xu, Q.; Hossain, A.M.S.; Jiang, D.-L.; Li, D.; Zhu, J.-J. Synergistically integrated Co_9S_8@NiFe-layered double hydroxide core-branch hierarchical architectures as efficient bifunctional electrocatalyst for water splitting. *J. Colloid Interf. Sci.* **2021**, *604*, 680–690. [CrossRef]
42. Su, L.; Cui, X.-Z.; He, T.; Zeng, L.-M.; Tian, H.; Song, Y.-L.; Qi, K.; Xia, B.-Y. Surface reconstruction of cobalt phosphide nanosheets by electrochemical activation for enhanced hydrogen evolution in alkaline solution. *Chem. Sci.* **2019**, *10*, 2019–2024. [CrossRef]
43. Ye, L.; Zhang, Y.-Q.; Wang, L.-M.; Zhao, L.-X.; Gong, Y.-Q. Assembly of ZIF-67 nanoparticles and in situ grown $Cu(OH)_2$ nanowires serves as an effective electrocatalyst for oxygen evolution. *Dalton Trans.* **2021**, *50*, 7256–7264. [CrossRef]
44. Zhang, B.; Qiu, C.-T.; Wang, S.; Gao, H.; Yu, K.-Y.; Zhang, Z.-F.; Ling, X.; Ou, W.; Su, C.-L. Electrocatalytic water-splitting for the controllable and sustainable synthesis of deuterated chemicals. *Sci. Bull.* **2021**, *66*, 562–569. [CrossRef]
45. Xie, C.; Zhang, X.; Matras-Postolek, K.; Yang, P. Hierarchical FeCo/C@$Ni(OH)_2$ heterostructures for enhanced oxygen evolution activity. *Electrochim. Acta* **2021**, *395*, 139194. [CrossRef]
46. Niu, S.-Q.; Sun, Y.-C.; Sun, G.-J.; Rakov, D.; Li, Y.-Z.; Ma, Y.; Chu, J.-Y.; Xu, P. Stepwise electrochemical construction of FeOOH/$Ni(OH)_2$ on Ni foam for enhanced electrocatalytic oxygen evolution. *ACS Appl. Energy Mater.* **2019**, *2*, 3927–3935. [CrossRef]
47. Wu, Q.; Dong, A.; Yang, C.; Ye, L.; Zhao, L.; Jiang, Q. Metal-organic framework derived Co_3O_4@Mo-Co_3S_4-Ni_3S_2 heterostructure supported on Ni foam for overall water splitting. *Chem. Eng. J.* **2021**, *413*, 127482. [CrossRef]
48. Guo, J.-X.; Zhang, K.; Sun, Y.-F.; Zong, Y.-X.; Guo, Z.-Y.; Liu, Q.Y.; Zhang, X.; Xia, Y.-Y. Enhanced hydrogen evolution of MoS_2/RGO: Vanadium, nitrogen dopants triggered new active sites and expanded interlayer. *Inorg. Chem. Front.* **2018**, *5*, 2092–2099. [CrossRef]
49. Xiao, L.; Bao, W.W.; Zhang, J.J.; Yang, C.M.; Ai, T.T.; Li, Y.; Wei, X.L.; Jiang, P.; Kou, L.J. Interfacial interaction between NiMoP and NiFe-LDH to regulate the electronic structure toward high-efficiency electrocatalytic oxygen evolution reaction. *Int. J. Hydrog. Energy* **2022**, *47*, 9230–9238. [CrossRef]
50. Gong, Y.; Zhi, Y.; Lin, Y.; Zhou, T.; Li, J.; Jiao, F.; Wang, W. Controlled synthesis of bifunctional particle-like Mo/Mn-Ni_xS_y/NF electrocatalyst for highly efficient overall water splitting. *Dalton Trans.* **2019**, *48*, 6718–6729. [CrossRef]
51. Bao, W.-W.; Xiao, L.; Zhang, J.-J.; Jiang, P.; Zou, X.-Y.; Yang, C.-M.; Hao, X.-L.; Ai, T.-T. Electronic and structural engineering of $NiCo_2O_4$/Ti electrocatalysts for efficient oxygen evolution reaction. *Int. J. Hydrog. Energy* **2021**, *46*, 10259–10267. [CrossRef]
52. Yu, M.-Q.; Li, X.-J.; Hua, G.-Y. Ultrathin nanosheets constructed $CoMoO_4$ porous flowers with high activity for electrocatalytic oxygen evolution. *Chem. Commun.* **2015**, *51*, 14361–14364. [CrossRef]

53. Dong, C.-L.; Yuan, X.-T.; Wang, X.; Liu, X.-Y.; Dong, W.-J.; Wang, R.-Q.; Duan, Y.-H.; Huang, F.-Q. Rational design of cobalt–chromium layered double hydroxide as a highly efficient electrocatalyst for water oxidation. *J. Mater. Chem. A* **2016**, *4*, 11292–11298. [CrossRef]
54. Li, J.; Li, G.-S.; Wang, J.-H.; Xue, C.-L.; Li, X.-S.; Wang, S.; Han, B.-Q.; Yang, M.; Li, L.P. A novel core–double shell heterostructure derived from a metal–organic framework for efficient HER, OER and ORR electrocatalysis. *Inorg. Chem. Front.* **2020**, *7*, 191–197. [CrossRef]
55. Cheng, P.-F.; Yuan, C.; Zhou, Q.-W.; Hu, X.-B.; Li, J.; Lin, X.-Z.; Wang, X.; Jin, M.-L.; Shui, L.-L.; Gao, X.-S.; et al. Core–Shell MoS_2@CoO electrocatalyst for water splitting in neural and alkaline solutions. *J. Phys. Chem. C* **2019**, *123*, 5833–5839. [CrossRef]
56. He, F.; Liu, Y.-J.; Ca, Q.-H.; Zhao, J.-X. Size-dependent electrocatalytic activity of ORR/OER on palladium nanoclusters anchored on defective MoS_2 monolayers. *New J. Chem.* **2020**, *44*, 16135–16143.
57. Nai, J.-W.; Yin, H.-J.; You, T.-T.; Zheng, L.-R.; Zhang, J.; Wang, P.-X.; Jin, Z.; Tian, Y.; Liu, J.Z.; Tang, Z.Y.; et al. Efficient electrocatalytic water oxidation by using amorphous Ni-Co double hydroxides nanocages. *Adv. Energy Mater.* **2015**, *5*, 1401880. [CrossRef]
58. Hu, H.; Guan, B.-Y.; Xia, B.-Y.; Lou, X.-W. Designed formation of Co_3O_4/$NiCo_2O_4$ double-shelled nanocages with enhanced pseudocapacitive and electrocatalytic properties. *J. Am. Chem. Soc.* **2015**, *137*, 5590–5595. [CrossRef]
59. Paliwala, M.; Meher, S. Study of "Ni-doping" and "open-pore microstructure" as physico-electrochemical stimuli towards the electrocatalytic efficiency of Ni/NiO for the oxygen evolution reaction. *New J. Chem.* **2020**, *44*, 17507–17517. [CrossRef]
60. Dileep, N.; Vineesh, T.; Sarma, P.; Chalil, M.; Prasad, C.; Shaijumon, M. Electrochemically Exfoliated β-$Co(OH)_2$ Nanostructures for enhanced oxygen evolution electrocatalysis. *ACS Appl. Energy Mater.* **2020**, *3*, 1461–1467. [CrossRef]
61. Yan, K.-L.; Sheng, M.-L.; Sun, X.-D.; Song, C.; Cao, Z.; Sun, Y.-J. Microwave synthesis of ultrathin nickel hydroxide nanosheets with Iron incorporation for electrocatalytic water oxidation. *ACS Appl. Energy Mater.* **2019**, *2*, 1961–1968.
62. Mohanty, B.; Ghorbani-Asl, M.; Kretschmer, S.; Ghosh, A.; Guha, P.; Panda, S.; Jena, B.; Krasheninnikov, A.; Jena, B.K. MoS_2 quantum dots as efficient catalyst materials for the oxygen evolution reaction. *ACS Catal.* **2018**, *8*, 1683–1689. [CrossRef]